Nonresonant formation of H⁻ near unreconstructed Si(100) surfaces

Boyan Obreshkov and Uwe Thumm

James R. Macdonald Laboratory, Department of Physics, Kansas State University, Manhattan, Kansas 66506-2604, USA

We calculate *ab initio* the fraction of outgoing negative hydrogen ions that are normally incident on an unreconstructed Si(100) surface with kinetic energies between 50 and 150 eV. The ground-state electronic structure of the surface is derived from a self-consistent screened Thomas–Fermi–von Weizsäcker pseudopotential including Wang-Teter shell structure corrections. Orbitals and energies of the electronic states in this potential are obtained by solving Kohn-Sham equations. The dynamics of the transfer of a single electron during the ion-surface collision is represented within the Newns-Anderson model, including image-charge interactions and electron translation factor. We show that the outgoing H⁻ fraction evolves at large distances from the surface due to nonresonant transitions from the valence band levels of the substrate into the affinity level of H⁻. In particular, we show that electron capture from dangling-bond surface-state resonances determines the final negative-ion fraction. We find good qualitative agreement with the experimental results of Maazouz *et al.* [Surf. Sci. **398**, 49 (1998)] for the scattering of hydrogen atoms and ions on silicon surfaces, even though our calculations do not include the effects of reconstruction and projectile motion parallel to the surface.

PACS number(s): 34.50.Dy, 34.70.+e, 79.20.Rf, 31.15.Ew

I. INTRODUCTION

Experiments on the scattering of hydrogen atoms on Si and Al surfaces [1] have measured the outgoing fractions of H⁻ ions. It was found that the negative-ion fraction on Si has the same magnitude as for Al surfaces. The relatively small variation in the observed final H⁻ fractions is interpreted by the authors in terms of different electronic structures of the two surfaces. For Al targets, the authors explain their observation within a free-electron model for the surface, in which the negative-ion fraction is formed on the outgoing part of the scattering trajectories, where electron loss to the conduction band and parallel velocity dependent electron capture from the Fermi sea of the substrate are competing. For Si targets, the authors invoke an indirect mechanism of formation involving dangling-bond surface states. While for metal surfaces, such as Al, there is excellent agreement between theory [2] and experiment, the theoretical description of the charge transfer near semiconductor surfaces is less developed. A recent *ab initio* theoretical approach [3] provided negative-ion fractions on (2×1) and (7×7) reconstructed Si surfaces in fair quantitative agreement with experiment [1]. In particular, it was found that details of the electronic structure of Si surfaces are better revealed as the parallel component of the impact velocity becomes smaller.

The neutralization of H⁻ ions near free-electron surfaces, such as aluminum, is well understood [2,4]. Aluminum does not exhibit a significant band gap, and the screening response of the electrons to the true nonuniformity of the crystal field of the ions is of little importance. Due to the loss of memory of the initial charge state prior to reflection from the surface, H⁻ formation occurs on the outgoing part of the scattering trajectory. Resonant electron loss to the conduction band will deplete the H⁻ population on exit from the surface, while resonant capture from the occupied valence band will be less efficient, due to the work function of Al ($W = 4.3$ eV) being large compared to the binding energy of the affinity level of

the negative ion ($E_a = -0.75$ eV). However, at nearly grazing incidence, when the projectile has a dominant parallel velocity component $\mathbf{v}_\parallel$, the situation is different. This is best understood in the rest frame of the projectile, where the velocities of the substrate electrons acquire a Galilean boost, translating the Fermi sphere of the occupied valence states by $\mathbf{v}_\parallel$. Hence resonant electron capture from kinematically shifted levels above the Fermi level occurs at large distances from the surface, such that the production of negative ions can compete with electron loss.

In the case of a semiconductor silicon surface, the situation is different due to the existence of an energy gap that separates valence from conduction bands. Due to the presence of the band gap, the density of states near the Fermi level is altered relative to the free-electron surface. This non-free-electron character of the substrate needs to be adequately represented in realistic charge-transfer calculations.

The objective of this work is to clarify the influence of the detailed electronic structure of the target on the outgoing H⁻ fraction under backscattering conditions, i.e., when the incoming H⁻ ions are normally incident to the surface and reflect specularly. Based on a density-functional description of the surface electronic structure and a Newns-Anderson single-active-electron representation of the charge-exchange dynamics between the surface and the incident projectile, we have developed a new scheme for the calculation of charge transfer near *arbitrarily* structured solid surfaces. In this work we show first numerical *ab initio* results for the example of H⁻ ions interacting with Si(100) surfaces. The physical (100) surface of the Si crystal undergoes reconstruction to a (2×1) superlattice. In view of (i) the unknown relevance of amorphization effects in scattering experiments on silicon surfaces [3], (ii) in order to provide first numerical results of our approach for a relatively simple (unreconstructed) surface morphology while retaining the most relevant features of the Si electronic structure, and (iii) with regard to trajectory-average effects that tend to weaken the
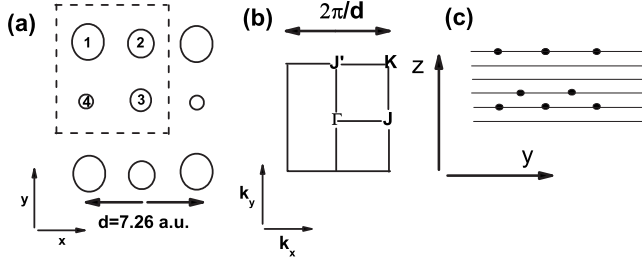
FIG. 1. (a) Orientation of the first four atomic planes of an unreconstructed Si(100) surface, viewed from the vacuum side normal to the surface toward the bulk. The atoms are shown as circles. The numbers in the circles label the atomic layers. The size of the circles indicates how far the atoms are from the vacuum interface. The spacing between the layers is $a_0/4$, where $a_0 = 10.263$ a.u. is the bulk lattice constant for Si. The area of the surface unit cell (dashed line) is the square of edge length $d = a_0/\sqrt{2}$. (b) Surface Brillouin zone corresponding to the planar unit cell. The irreducible quarter of the zone with the four high symmetry points is also shown. (c) Cut of the unreconstructed Si(100) surface along a plane parallel to the y-z plane and perpendicular to the surface, intersecting atoms with labels 1 and 4 in (a). Our numerical examples in Figs. 2, 4, and 5 below refer to this cut. Dots indicate the positions of Si cores.

sensitivity of the final charge state of surface-scattered ions on the detailed surface morphology, we disregard surface reconstruction in this work. As we will demonstrate, valuable insight into the charge-transfer dynamics can be obtained from this study of the model unreconstructed Si surface. Therefore, we first calculate the ground-state electronic structure of an unreconstructed Si(100) surface from an extended Thomas–Fermi–von Weizsäcker (TFvW) method, using an empirical local pseudopotential for the description of the ionic cores. We derive an orbital-free single-particle electronic potential. Next, we obtain orbitals and energies of the target electronic states by solving Kohn-Sham equations. The perturbation of these orbitals by the incident H$^-$ ion is described within the Newns-Anderson model. Our calculations were done for kinetic energies of the incoming H$^-$ ions between 50 and 150 eV.

The plan of this paper is as follows. In Sec. II we describe the theoretical scheme of our calculations. In Sec. III we present and discuss both, the numerical results for the static electronic structure of the target and the electron-exchange dynamics. Section IV contains our main conclusion. Unless stated otherwise, we use atomic units ($e = \hbar = m_e = 1$).

II. THEORETICAL FORMULATION

Figures 1(a) and 1(c) illustrate the geometry of the unreconstructed (1×1) Si(100) surface employed in our calculations. The surface Brillouin zone (SBZ), together with its irreducible quarter, is shown in Fig. 1(b).

A. Surface electronic structure

To calculate the equilibrium valence electronic structure of the surface, we use a 13-layer slab of Si atoms with six

layers of vacuum added on top of the surfaces on both sides. The height of the slab is $H = 25a_0/4$, where $a_0 = 10.263$ is the bulk lattice constant of Si. The total ground-state energy density functional for the valence electrons is [5]

$$E[n] = T_s[n] + \frac{1}{2} \int d^3\mathbf{r}\, d^3\mathbf{r}' \frac{n(\mathbf{r})n(\mathbf{r}')}{|\mathbf{r} - \mathbf{r}'|} + E_{\mathrm{xc}}^{\mathrm{LDA}}[n]$$
$$+ \int d^3\mathbf{r}\, v_{\mathrm{core}}(\mathbf{r})n(\mathbf{r}), \tag{1}$$

where $n(\mathbf{r})$ is the electron density. T_s is the kinetic energy of an auxiliary system of noninteracting electrons. The second term is the repulsive electrostatic Coulomb energy for the electrons, $E_{\mathrm{xc}}^{\mathrm{LDA}}$ is the exchange-correlation energy in local density approximation, and v_{core} is the potential field of the ionic cores of the crystal. The unscreened pseudopotential of the Si ionic cores with charge $Z = 4$ is

$$v_{\mathrm{core}}(\mathbf{r}) = \sum_{I=1}^{N} v_{\mathrm{ps}}(\mathbf{r} - \mathbf{R}_I), \tag{2}$$

where N is the total number of cores with position vectors $\{\mathbf{R}_I\}$ enclosed in a unit cell of volume Ω. We use an empirical local pseudopotential v_{ps} from Ref. [6]. In momentum space it is given by

$$\tilde{v}_{\mathrm{ps}}(q) = 4\pi Z F(q)/q^2. \tag{3}$$

The function $F(q) = [\cos(a_1 q) + a_2]e^{a_3 q^4}/(1 + a_2)$ is the form factor of the core and takes into account the Pauli repulsion between the valence and core electrons, which is formally expressed by the short wavelength cutoff of the unscreened Coulombic core potential. Values for the pseudopotential parameters for Si are $\{a_1 = 0.791, a_2 = -0.352, a_3 = -0.018\}$. We approximate the noninteracting kinetic energy T_s as the sum of the Thomas-Fermi local density approximation, the von Weizsäcker term with gradient parameter λ_{vW}, and a nonlocal correction introduced by Wang and Teter [7],

$$T_s[n] = \int_{\Omega} d^3\mathbf{r} \left(\frac{3}{10}(3\pi^2)^{2/3} n^{5/3}(\mathbf{r}) + \frac{1}{8}\frac{|\nabla n(\mathbf{r})|^2}{n(\mathbf{r})} \right) + T_{\mathrm{WT}}[n], \tag{4}$$

where the Wang-Teter kinetic energy shift is given by [7–10]

$$T_{\mathrm{WT}}[n] = \int_{\Omega} d^3\mathbf{r} \int_{\Omega} d^3\mathbf{r}'\, K_s(|\mathbf{r} - \mathbf{r}'|)\delta n^{(5/6)}(\mathbf{r})\delta n^{(5/6)}(\mathbf{r}')$$
$$+ \int_{\Omega} d^3\mathbf{r} \int_{\Omega} d^3\mathbf{r}' \int_{\Omega} d^3\mathbf{r}''\, L_s(|\mathbf{r} - \mathbf{r}'|, |\mathbf{r} - \mathbf{r}''|)$$
$$\times \delta n^{(5/9)}(\mathbf{r})\delta n^{(5/9)}(\mathbf{r}')\delta n^{(5/9)}(\mathbf{r}''). \tag{5}$$

Equation (5) is an expansion over fractional powers of the deviation $\delta n^{(z)}(\mathbf{r}) = n^z(\mathbf{r}) - n_0^z$ from the average electron density in the system $n_0 = NZ/\Omega$. The exponents $z = 5/6$ and 5/9 comply with the correct transformation of the functional under uniform scaling of the spatial coordinates $\mathbf{r} \rightarrow \gamma\mathbf{r}$, given by $T_s[n(\gamma\mathbf{r})] = \gamma^2 T_s[n]$. This expansion emphasizes the perturbative origin of the Wang-Teter kinetic energy, and there-

fore its applicability is limited to systems with relatively weak ionic pseudopotentials. The functional T_{WT} is not positively defined, which is a drawback of our model. However, the total kinetic energy of the gas is dominated by the non-perturbative Thomas–Fermi–von Weizsäcker part, which is positively defined and provides a strict upper limit to the exact kinetic energy of the noninteracting gas [11].

The single-particle two- and three-point static response kernels K_s and L_s represent more accurately the screening of the pseudopotential at intermediate wavelengths $\lambda \sim 2\pi/k_F$. $k_F = (3\pi^2 n_0)^{1/3}$ is the Fermi momentum corresponding to the average electron density n_0. The kinetic energy density functional (4) becomes exact in the limit of a uniform free-electron gas, perturbed by a weak static potential. In this case the induced screening electron density relative to n_0 to second order in v_{core} can be written as

$$\delta n_s(\mathbf{q}) = \chi_s(q) v_{\text{core}}(\mathbf{q}) + \sum_{\mathbf{q}_1, \mathbf{q}_2} \delta(\mathbf{q}_1 + \mathbf{q}_2 - \mathbf{q})$$

$$\times \frac{I_s(q_1, q_2, q)}{\pi^2 k_F} v_{\text{core}}(\mathbf{q}_1) v_{\text{core}}(\mathbf{q}_2), \tag{6}$$

where χ_s and I_s are the linear and quadratic response functions for the homogeneous free-electron gas. According to the Kohn-Sham theorem [12], Eq. (6) also gives the induced density for the interacting electron gas, i.e., $\delta n(\mathbf{q}) = \delta n_s(\mathbf{q})$. Alternatively, Eq. (6) can be derived from the Euler equation $\delta E / \delta n = \text{const}$, using the representation (4) for the kinetic energy [7]. The comparison of both expressions determines the functional form of the screening kernels K_s and L_s. The Fourier transform of K_s is given by

$$\tilde{K}_s(q) = -\frac{18}{25} n_0^{1/3} [\chi_s^{-1}(x) - \chi_{\text{TF}}^{-1} - \chi_{\text{vW}}^{-1}(x)], \tag{7}$$

where

$$\chi_s(x) = \frac{1}{2} + \frac{x^2 - 4}{8x} \ln \left| \frac{2 - x}{2 + x} \right|, \quad x = q/k_F \tag{8}$$

is the static limit of the Lindhard density response function [11,13], $\chi_{\text{TF}} = k_F/\pi^2$ is the Thomas-Fermi limit of χ_s at long wavelengths $(q \to 0)$, and $\chi_{\text{vW}} = 4k_F/3\pi^2(q/k_F)^2$ is the von Weizsäcker limit for the screening response of the free-electron gas to a weak and rapidly varying $(q \gg k_F)$ external potential. The inclusion of the linear response correction is an important improvement over the TFvW kinetic energy since it extrapolates the response properties of the true non-uniform electron gas to the intermediate range of momentum transfers. It includes the weak logarithmic singularity of χ_s at $q = 2k_F$, which is related to the long-range Friedel oscillations of the electron density [5]. The application of quadratic response theory gives results in the Fourier transform of L_s [7,8,14],

$$\tilde{L}_s(q_1, q_2, q_3) = \frac{729}{125\Omega^2 n_0^{2/3}} \left\{ \frac{k_F^2}{18} + \frac{k_F^2}{16} \sum_{i=1}^{3} x_i^2 + \frac{25}{648} \Omega n_0^{2/3} \right.$$

$$\times [\tilde{K}_s(x_1) + \tilde{K}_s(x_2) + \tilde{K}_s(x_3)]$$

$$\left. + \frac{k_F^5}{27\pi^6} \chi_s^{-1}(x_1) \chi_s^{-1}(x_2) \chi_s^{-1}(x_3) I_s(x_1, x_2, x_3) \right\}, \tag{9}$$

where $x_i = q_i/k_F$. If $q_1 + q_2 = q_3$, the function I_s is given by

$$I_s(q_1, q_2, q_3) = \frac{-\pi^2 k_F^2}{6 x_1 x_2 x_3} [x_1 \chi_s(x_1) + x_2 \chi_s(x_2) - x_3 \chi_s(x_3)], \tag{10}$$

otherwise, for $\mathbf{q}_1 + \mathbf{q}_2 + \mathbf{q}_3 = 0$, it is given by

$$I_s(q_1, q_2, q_3) = U(\mathbf{q}_1, \mathbf{q}_2) + U(\mathbf{q}_1, \mathbf{q}_3) + U(\mathbf{q}_2, \mathbf{q}_3). \tag{11}$$

The function U has a discontinuity at $x_3^2 = 4 \sin^2 \theta$. For $x_3^2 - 4 \sin^2 \theta \geq 0$ it is

$$U(\mathbf{q}_1, \mathbf{q}_2) = \frac{1}{4 x_1 x_2 \sin^2 \theta} \left\{ (x_1 \cos \theta + x_2) \ln \left| \frac{2 + x_1}{2 - x_1} \right| \right.$$

$$+ (x_2 \cos \theta + x_1) \ln \left| \frac{2 + x_2}{2 - x_2} \right| + \sqrt{x_3^2 - 4 \sin^2 \theta}$$

$$\left. \times \ln \left| \frac{4 \cos \theta + x_1 x_2 - 2\sqrt{x_3^2 - 4 \sin^2 \theta}}{4 \cos \theta + x_1 x_2 + 2\sqrt{x_3^2 - 4 \sin^2 \theta}} \right| \right\}, \tag{12}$$

where θ is the relative angle between $\mathbf{q}_1$ and $\mathbf{q}_2$, while for $x_3^2 - 4 \sin^2 \theta \leq 0$,

$$U(\mathbf{q}_1, \mathbf{q}_2) = \frac{1}{4 x_1 x_2 \sin^2 \theta} \left\{ (x_1 \cos \theta + x_2) \ln \left| \frac{2 + x_1}{2 - x_1} \right| \right.$$

$$+ (x_2 \cos \theta + x_1) \ln \left| \frac{2 + x_2}{2 - x_2} \right| + \sqrt{4 \sin^2 \theta - x_3^2}$$

$$\left. \times \left[\pi + \arctan \frac{-2\sqrt{4 \sin^2 \theta - x_3^2}}{x_1 x_2 + 4 \cos \theta} \right] \right\}. \tag{13}$$

We use the local density approximation (LDA) for the exchange-correlation energy as in our earlier studies [15]. In particular, we use the Dirac approximation for the exchange energy and Wigner's interpolation formula for the correlation energy of the electron gas. The variational Euler equation for the equilibrium ground-state electron density, subject to the constraint that the total number of electrons be conserved and equal to NZ, is

$$\frac{\delta E}{\delta n(\mathbf{r})} - \mu = 0, \tag{14}$$

where μ is the chemical potential of the electron gas.

After making the substitution $n(\mathbf{r}) = \psi^2(\mathbf{r})$ in Eq. (14), the ground-state properties of the electronic system are reexpressed in terms of a one-body "wave function" of the electron density, which satisfies the nonlinear Schrödinger equation

$$\left(-\frac{1}{2}\nabla^2 + v_{\text{eff}}[\psi;\mathbf{r}] - \mu\right)\psi(\mathbf{r}) = j_s[\psi;\mathbf{r}], \qquad (15)$$

with an effective single-particle potential

$$v_{\text{eff}}(\mathbf{r}) = v_{\text{TF}}(\mathbf{r}) + v_H(\mathbf{r}) + v_{\text{core}}(\mathbf{r}) + v_{\text{xc}}^{\text{LDA}}(\mathbf{r}). \qquad (16)$$

The Thomas-Fermi term

$$v_{\text{TF}}(\mathbf{r}) = \frac{1}{2}(3\pi^2)^{2/3}\psi^{4/3}(\mathbf{r}) \qquad (17)$$

is repulsive for the valence electrons due to Pauli's exclusion principle, and the electrostatic Hartree potential is

$$v_H(\mathbf{r}) = \int d^3\mathbf{r}' \frac{\psi^2(\mathbf{r}')}{|\mathbf{r} - \mathbf{r}'|}. \qquad (18)$$

The last two terms in Eq. (16) are the bare unscreened pseudopotential of the ionic cores $v_{\text{core}}(\mathbf{r})$ and the exchange-correlation potential $v_{\text{xc}}^{\text{LDA}}(\mathbf{r}) = \delta E_{\text{xc}}^{\text{LDA}}[n]/\delta n(\mathbf{r})$ in LDA. The right-hand side of Eq. (15) is the nonlinear Wang-Teter shell-structure term $j_s[\psi,\mathbf{r}] = -\psi(\mathbf{r})\delta T_{\text{WT}}/\delta n(\mathbf{r})$. Equation (15) is solved by iteration using a 3D FFT method. Details about the numerical scheme are given in Appendix A.

B. Charge-transfer dynamics

The converged orbital-free potential is used to solve the Schrödinger equation for the stationary noninteracting single particle states

$$\left(-\frac{1}{2}\nabla_{\mathbf{r}}^2 + v_s(\mathbf{r})\right)\varphi_{\nu,\mathbf{k}_\parallel}(\mathbf{r}) = \varepsilon_\nu(\mathbf{k}_\parallel)\varphi_{\nu,\mathbf{k}_\parallel}(\mathbf{r}), \qquad (19)$$

where $v_s = v_{\text{core}} + v_H + v_{\text{xc}}^{\text{LDA}}$ is the local Kohn-Sham potential, ν is a band index, and $\mathbf{k}_\parallel$ is the conserved parallel Bloch quasimomentum. Equation (19) is integrated numerically using the Car-Parrinello method [16] for a large number of Bloch waves in the irreducible quarter of the SBZ, as described in more detail in Appendix B. After diagonalization of the Kohn-Sham Hamiltonian (19), we describe the dynamics of the electron charge transfer between the incident H⁻ ion and the surface within the Newns-Anderson model [17], based on the Hamiltonian

$$H(t) = \varepsilon_a(t)c_a^\dagger(t)c_a(t) + \sum_k \varepsilon_k c_k^\dagger(t)c_k(t)$$

$$+ \left(\sum_k V_{ak}(t)c_a^\dagger(t)c_k(t) + \text{H.c.}\right), \qquad (20)$$

where $k = \{\nu, \mathbf{k}_\parallel, \sigma\}$ denotes the quantum numbers of the Kohn-Sham states, σ is the projection of the electron spin on the surface normal, c_a, c_k are the annihilation operators of the anion and semiconductor states, $\varepsilon_a, \varepsilon_k$ are the corresponding orbital energies, and $V_{ak}(t)$ are the matrix elements for trans-

fer of one electron from the surface to the anion. The couplings V_{ak} between target and projectile states are evaluated using the expansion

$$V_{ak}(t) = \frac{\delta_{\sigma,\sigma'}}{\sqrt{\Omega}} \sum_{\mathbf{G}} c_{\nu,\mathbf{k}_\parallel + \mathbf{G}} \langle a|V_{e\text{-H}}|\mathbf{G} + \mathbf{k}_\parallel - \mathbf{v}(t)\rangle$$

$$\times e^{i[\mathbf{G} + \mathbf{k}_\parallel - \mathbf{v}(t)]\cdot\mathbf{D}(t)} \qquad (21)$$

over the reciprocal-lattice wave vectors $\mathbf{G} = 2\pi(l/d, m/d, n/H)$, where (l, m, n) are integer numbers. $\mathbf{D}(t)$ is the classical trajectory of the center-of-mass of the projectile relative to the surface, and $\mathbf{v}(t)$ is the collision velocity. The adiabatic dependence of the matrix elements on the impact velocity is a consequence of the Galilei transformation of the atomic wave function to the rest frame of the surface.

We use the electron-hydrogen interaction potential $V_{e\text{-H}}$ of Ref. [18],

$$V_{e\text{-H}}(r) = -(1 + 1/r)e^{-2r} - (\alpha_H/2)e^{-r_0^2/r^2}/r^4, \qquad (22)$$

where r is the relative distance between the electron and the projectile, $\alpha_H = 4.5$ is the ground-state polarizability of the hydrogen atom, and $r_0 = 1.2$. The potential (22) holds a single weakly bound affinity level with energy $\varepsilon_a = 0.75$ eV below the vacuum level. This potential becomes unreliable at close distances to the surface, because of the strong overlap between the substrate with the adsorbate atom.

The equations of motion for the annihilation operators of electronic states are given by

$$i\partial_t c_q(t) = [c_q(t), H(t)], \qquad (23)$$

where $q = \{a, k\}$. In explicit form we have

$$i\partial_t c_a(t) = \varepsilon_a(t)c_a(t) + \sum_k V_{ak}(t)c_k(t),$$

$$i\partial_t c_k(t) = \varepsilon_k c_k(t) + V_{ak}^*(t)c_a(t). \qquad (24)$$

We note that our numerical approach does not account for the orthogonalization of the atomic orbital a to the substrate orbitals k. The significance of this effects can be studied only in a separate calculation, which is beyond the scope of the present work. The formal integration of Eqs. (24) for the band operators gives an equation for the annihilation operator of the H⁻ state

$$i\partial_t c_a(t) = \varepsilon_a(t)c_a(t) + \int_{t_0}^t dt' \Sigma_r(t, t')c_a(t')$$

$$+ \sum_k V_{ak}(t)e^{-i\varepsilon_k(t-t_0)}c_k(t_0), \qquad (25)$$

where the retarded self-energy of the negative ion affinity level is

$$\Sigma_r(t, t') = -i\theta(t - t')\sum_k V_{ak}(t)e^{-i\varepsilon_k(t-t')}V_{ak}^*(t'). \qquad (26)$$

By expanding the interacting operator $c_a(t)$ over noninteracting annihilation operators [19],
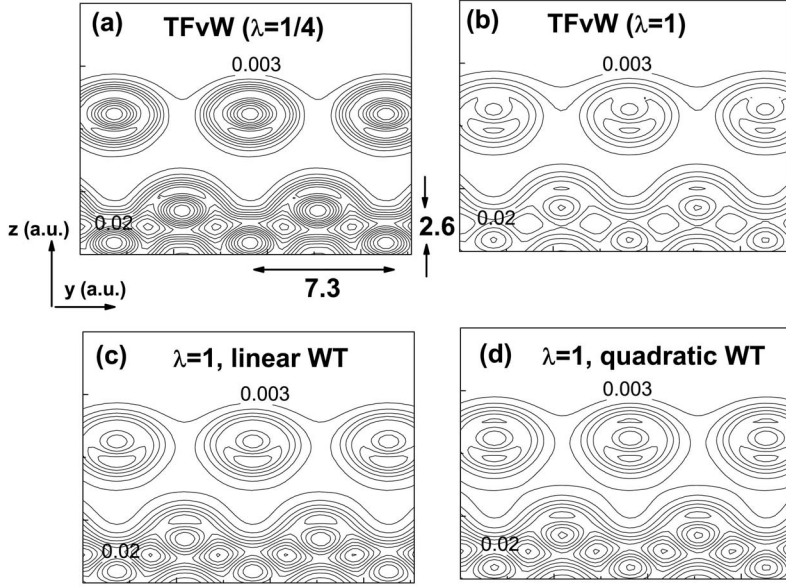
FIG. 2. Contour map of the orbital-free valence electron density of the unreconstructed Si(100) surface along the plane shown in Fig. 1(c). All graphs show the vacuum interface on top and extend six layers into the bulk. (a) TFvW ($\lambda_w=1/4$) model, (b) TFvW ($\lambda_w=1$) model, (c) TFvW ($\lambda_w=1$) model, including linear Wang-Teter screening corrections, and (d) TFvW ($\lambda_w=1$) model, including linear and quadratic Wang-Teter corrections. The contour line spacing is 0.003 a.u. The distance between adjacent atoms along the y axis, and the interlayer spacing along the z axis of the surface are indicated in (a).

$$c_a(t) = S_{aa}(t,t_0)c_a(t_0) + \sum_k S_{ak}(t,t_0)c_k(t_0), \quad (27)$$

substituting the result in Eq. (25), multiplying on the left by the adjoint noninteracting creation operators, taking the expectation value in the initial state $|t_0\rangle$ of the electrons, and using that $\langle t_0|c_q^\dagger(t_0)c_{q'}(t_0)|t_0\rangle = n_q\delta_{qq'}$, n_q being the interaction-free occupation numbers of electronic states, we obtain a set of decoupled equations for the amplitudes of ion survival in the initial state $S_{aa}=\langle a,t|a,t_0\rangle$ and capture from a crystal band $S_{ak}=\langle a,t|k,t_0\rangle$,

$$i\partial_t S_{aa}(t) = \int dt' \widetilde{\Sigma}_r(t,t')S_{aa}(t'),$$

$$i\partial_t S_{ak}(t) = \int dt' \widetilde{\Sigma}_r(t,t')S_{ak}(t') + \widetilde{V}_{ak}(t). \quad (28)$$

The self-energy kernel

$$\widetilde{\Sigma}_r(t,t') = -i\theta(t-t')\sum_k \widetilde{V}_{ak}(t)\widetilde{V}_{ak}^*(t') \quad (29)$$

is expressed in terms of matrix elements of the hydrogenic-core potential as

$$\widetilde{V}_{ak}(t) = e^{iA(t,t_0)}V_{ak}(t)e^{-i\varepsilon_k(t-t_0)}. \quad (30)$$

$A(t,t_0)$ is the classical action of the negative ion affinity energy level $\varepsilon_a(t)$ along the trajectory of the projectile, which is shifted due to the static long-range image-charge interactions, and includes adiabatically a kinematic shift due to the Galilei transformation of the atomic wave function to the rest frame of the surface, i.e.,

$$A(t,t_0) = \int_{t_0}^t d\tau \varepsilon_a(\tau) = \varepsilon_a(t-t_0) + \int_{t_0}^t d\tau \frac{|\mathbf{v}(\tau)|^2}{2}$$

$$- \frac{1}{4}\frac{\varepsilon_b-1}{\varepsilon_b+1}\int_{t_0}^t \frac{d\tau}{D(\tau)+\lambda_s}. \quad (31)$$

The static bulk dielectric constant of Si is $\varepsilon_b \approx 12$ [20], the surface plasmon wavelength $\lambda_s \approx n_0^{-1/6}$ is introduced as a cut-off distance, and the separation between the projectile and the surface is $D(t)$. The probability to find the H⁻ affinity level occupied after the collision is

$$P_a(\infty) = |S_{aa}(\infty,-\infty)|^2 + \sum_{\nu,\mathbf{k}_\parallel} n_k|S_{ak}(\infty,-\infty)|^2, \quad (32)$$

where $n_k = \theta(\varepsilon_F - \varepsilon_k)$ are the occupation numbers of the semiconductor band states prior to the collision. Some details for the numerical solution of Eqs. (28) for the transition amplitudes are given in Appendix C.

III. NUMERICAL RESULTS AND DISCUSSION

The ground-state electronic properties of the surface and single-particle potentials are discussed in Sec. III A. In Sec. III B we show results for the ion-charge fractions for incident H⁻ projectiles with kinetic energies between 50 and 150 eV.

A. Electronic structure calculation

Our orbital-free calculations were done for four different models for the screening response in the electron gas. In the first two models we neglect the Wang-Teter response corrections. First, we solve the "TFvW model" with gradient parameter $\lambda_w=1/4$ as in our earlier studies [15,21]. In the second model the strength of the von Weizsäcker term is increased to $\lambda_w=1$. The last two models include the Wang-Teter corrections to the TFvW functional with gradient parameter $\lambda_w=1$. In particular, the third model is extended to include the linear response screening corrections (we will

refer to this model as the "linear WT model"), while the fourth model includes the full Wang-Teter kinetic energy (referred to as the "quadratic WT model").

Figure 2 shows the contour map of the electron densities corresponding to the four orbital-free models as outlined above. The common feature is obvious. In the bulk of the crystal the electrons avoid the repulsive Pauli forbidden regions and instead distribute in between the cores, forming covalent bond charges. Near the surface the screening of the pseudopotential is anisotropic, i.e., the electron density spills out towards the vacuum at a distance of about $\lambda_F/2 \approx 4$ from the jellium edge (located at half a lattice spacing in front of the first surface layer). $\lambda_F = 2\pi/k_F$ is the Fermi wavelength. In the opposite direction a polarization cloud forms at the bulk side of the surface atoms. The resulting surface dipole layer exhibits an asymmetry with respect to the position of the jellium edge.

The TFvW ($\lambda_w = 1/4$) density shown in Fig. 2(a) is highly localized near individual atoms. The valence electron distribution near the surface is rigid and exhibits a steep gradient in vacuum direction, while the bridge to the bulk is provided by the presence of polarization charges near the interior side of the surface atoms. This polarization cloud exhibits the highest degree of localization among the four different models. As a consequence of this distribution, the surface pseudopotential is very efficiently screened, and valence electrons in the surface region do not gain much potential energy by interacting with the bulk lattice of Si ionic cores. After increasing the strength of the gradient parameter to its limiting value $\lambda_w = 1$, as shown in Fig. 2(b), the density exhibits a higher degree of uniformity near the surface and in the bulk. Because of this uniformity of the TFvW ($\lambda_w = 1$) electron distribution, the ionic pseudopotential remains highly unscreened. The amplitudes of the bulk interstitial charges have decreased by more than 20%, since the electrons redistribute and fill the core regions of the crystal. This filling of the core regions is even more efficient near the surface, and is accompanied by (i) the depletion of the outer regions of the atoms, (ii) a uniform spilling out of electrons to the vacuum, and (iii) the expansion of the polarization cloud at the bulk side of the surface atoms.

The inclusion of the linear response WT corrections improves the highly uniform TFvW ($\lambda_w = 1$) electron density near the surface and in the bulk [Fig. 2(c)]. The bulk electrons partially deplete the core regions and increase their presence in the interstitial bonding and interlayer regions. In response to this redistribution, the surface density also changes and part of the electronic cloud delocalizes towards the bulk. The quadratic WT density is shown in Fig. 2(d). The amplitudes of the bulk bonding charges have slightly increased, and the filling of the cores is more uniform. The tendency of the electrons to delocalize in between the atomic planes is more evident than in the linear WT model. A similar spill out of electronic density occurs near the surface atoms.

The distinct characteristics of the surface electronic density in the four different models lead to different contributions to the potential difference across the surface dipole layer $d_{es} = \bar{\phi}_b - \phi_{vac}$ and hence to the work function $W = d_{es}$
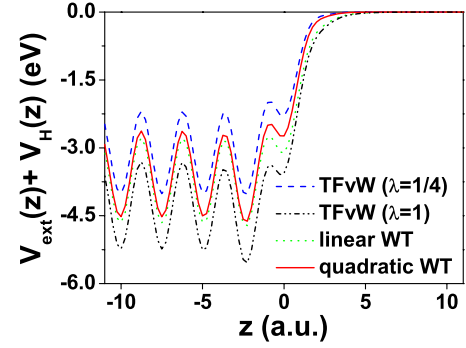

FIG. 3. (Color online) Variation of the electrostatically screened ionic pseudopotentials in direction normal to the unreconstructed Si(100) surface for the four different models for the screening response of the electron gas: TFvW ($\lambda = 1/4$) model, TFvW ($\lambda = 1$) model, linear Wang-Teter model, and quadratic Wang-Teter model (see text). The jellium edge is at $z = 0$.

$-\mu_b$. $\bar{\phi}_b$ is the mean electrostatic potential in the bulk, ϕ_{vac} is the vacuum electrostatic potential, and μ_b is the bulk chemical potential. In order to quantify this effect, we plot in Fig. 3 the electrostatically screened ionic potential, averaged over a surface-unit cell in the direction normal to the surface. The model-dependent work function is given in Table I in comparison with experimental results. Values for the surface dipole layer and bulk chemical potential are also shown.

The potential change in the dipole layer across the metal-vacuum interface is $d_{es} = 3$ eV as calculated from the TFvW ($\lambda_w = 1/4$) model. The TFvW ($\lambda_w = 1$) model predicts a significant increase of d_{es} by 1.5 eV (Table I and Fig. 3). The TFvW ($\lambda_w = 1/4$) model exhibits the lowest work function and underestimates by 1 eV the measured values in [22,23]. In contrast, the TFvW ($\lambda_w = 1$) work function overestimates the experiment by 0.7 eV. The bulk chemical potential has not changed much relative to the TFvW ($\lambda_w = 1/4$) prediction. Therefore, the large difference of the work function between the TFvW models is due to the electrostatic unscreening of the ionic pseudopotential as $\lambda_w \rightarrow 1$.

The linear and quadratic response corrections are depolarizing the surface and decreasing d_{es} by 0.9 eV, relative to the TFvW ($\lambda_w = 1$) model. This is due to the above-mentioned

TABLE I. Numerical results for the work function W of the Si(100) surface for four different models for the screening response of the electron gas compared with the measured work functions in Refs. [22,23]. The third and fourth columns show the potential-energy change d_{es} across the surface-dipole layer and the bulk chemical potential μ_b.

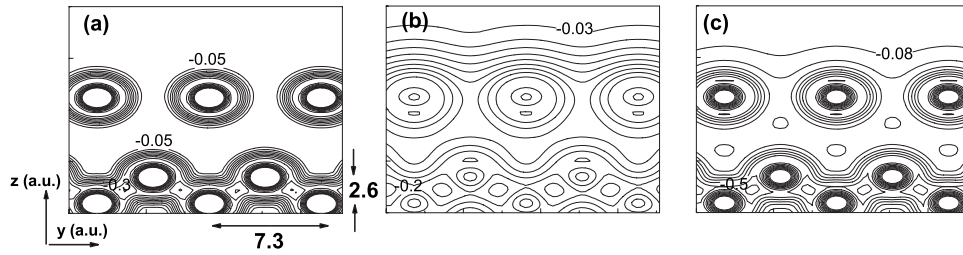| Model	W (eV)	d_{es} (eV)	μ_b (eV)
TFvW ($\lambda = 1/4$)	3.8	3.0	−0.8
TFvW ($\lambda = 1$)	5.5	4.5	−1.0
Linear WT	5.2	3.6	−1.6
Quadratic WT	4.1	3.6	−0.5
Experiment [22]	4.8		
Experiment [23]	4.7		

FIG. 4. Different contributions to the single-particle Kohn-Sham pseudopotential for the valence- and conduction-band electrons of an unreconstructed Si(100) surface along the plane shown in Fig. 1(c). All graphs show the vacuum interface on top and extend six layers into the bulk. (a) Hartree potential of the electronic and ionic-core charges $v_H + v_{core}$, (b) exchange-correlation potential in LDA, and (c) orbital-free Kohn-Sham potential. Only negative values of the potential relative to the vacuum energy level are shown. The contour line spacing is 0.05 a.u. (a), 0.03 a.u. (b), and 0.08 a.u.(c).

effect of delocalization of the electronic cloud relative to the structure of the crystal. However, the linear WT work function still exceeds the experimental values. The screening in the quadratic WT model is very efficient, and W is significantly lowered by 1.1 eV with respect to the linear model. Since the linear and quadratic WT screening corrections give the same contribution to the surface dipole layer, the relative difference for the work function in the WT models is due to the bulk chemical potential μ_b. Since we use the LDA for E_{xc}, the exchange-correlation part of μ_b is the same for all the models. Therefore the large work function change between the WT models is due to kinetic energy effects, imposed by the explicit nonlocality of the Wang-Teter kinetic energy density functional as a direct consequence of the Pauli exclusion principle.

Since the quadratic WT model does not overestimate the measured work function of the Si(100) surface and also provides a realistic absolute value for $W=4.1$ eV, it will be used in our further analysis. The different contributions to the self-consistent single-particle potential v_s for the quadratic WT model are shown in Fig. 4. The electrostatically screened ionic pseudopotential $v_H + v_{core}$ in Fig. 4(a) exhibits the structure of the crystal. It is repulsive for the electrons near the core regions, while the attractive screened Coulombic part has major influence in the bonding regions, where it has a peak amplitude of 7–8 eV. The exchange-correlation potential in Fig. 4(b) is the dominant component of the pseudopotential in the vacuum and interlayer regions of the crystal. In the interstitial bonding regions it has a similar magnitude, $v_{xc} \approx 7$ eV, as the screened Coulombic part of the pseudopotential. The full single-particle Kohn-Sham potential is shown in Fig. 4(c).

The wave functions of the electronic states in the screened pseudopotential are obtained by solving Kohn-Sham equations as described in Appendix B. The irreducible quarter of the SBZ was sampled for a large number of points $N_k = 80$, and the lowest 40 states per wave vector were obtained. A plane wave basis of size $(N_x, N_y, N_z) = (2^3, 2^3, 2^7)$ was used to represent electronic orbitals. As a result of the truncation of the bulk crystal, we find two dispersive unoccupied surface state bands, in good agreement with the theoretical results of Refs. [24,25]. The orbital densities of these states along the $\Gamma J'$ line, $\mathbf{k}_\parallel = (0, k_y)$, of the SBZ are shown in Fig. 5. The corresponding dispersion of the orbital energy as a function of the parallel momentum for these two bands is shown in Fig. 6 along the $J'\Gamma J$ contour in SBZ.

Figure 5(a) presents the orbital density of a dangling bond sp_z hybrid state, which is directed normal to the surface with a node below the atoms of the first atomic layer. The dimer-like bridge state in Fig. 5(b) has a p_y character and is confined to the first atomic layer in between adjacent surface atoms. The dangling-bond band exhibits weak dispersive features along the chosen contour and has a bandwidth of 0.8 eV. At the J' point, $\mathbf{k}_\parallel = (0, \pi/d)$, this state has sp_z character. By decreasing the crystal quasimomentum along the $J'\Gamma$ line, the orbital density smears among the atoms in the first atomic layer and rapidly decays into the bulk; at Γ this state is nearly degenerate with the valence band. The p_y bridge states are shown in Fig. 5(b) near the J' point. They exhibit pronounced dispersive features within a bandwidth of about 2.7 eV (Fig. 6); similarly their orbital density is distributed in between the Si cores as the momentum k_y decreases from 0.3 to 0.2. The bulk wave-vector contributions to this state are rapidly destroyed as k_y approaches the center of the SBZ, and a nodal structure evolves in between the atoms of the first atomic layer. Near the Γ point this band has merged into the conduction band. Both surface states exhibit weak dispersive features along the ΓJ line, $\mathbf{k}_\parallel = (k_x, 0)$. Corresponding orbitals are not shown. The comparison of our results for the band structure calculation with the results in Refs. [24,25] shows that the behavior of the two surface-state bands along the chosen lines in the SBZ exhibits a similar overall trend.

An important group of bulk states that influences the charge-transfer dynamics exhibit anomalous surface amplitudes in their densities. These surface-state resonances of dangling bond type are shown in Figs. 5(c) and 5(d) near the Γ point of SBZ. Inside the bulk, the orbital densities exhibit clear covalent bonding character. Near the vacuum-surface interface, the orbital densities gain amplitude above the surface atoms and protrude in the direction of the vacuum.

The total density of states calculated using 3200 electronic states,

$$\rho(E) = \frac{2}{\Omega} \sum_{\nu, \mathbf{k}_\parallel} \delta(E - \varepsilon_\nu(\mathbf{k}_\parallel)), \tag{33}$$

is shown in Fig. 7. Clearly there is a loss of spectral weight above the Fermi level, and an energy gap opens in between the valence and conduction bands. The surface-state bands reside in the gap region. The dangling-bond band is weakly
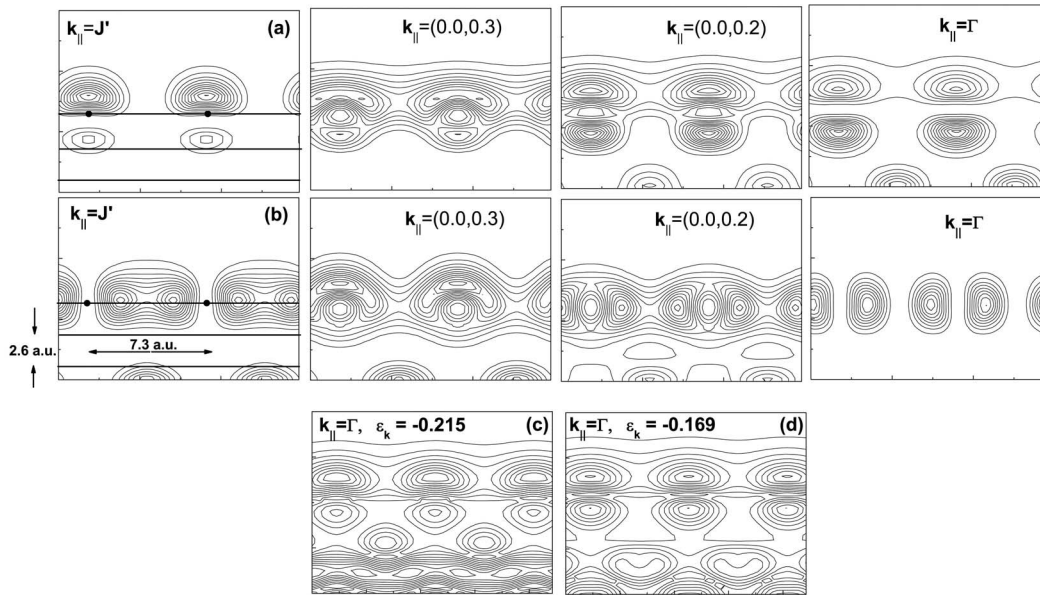
FIG. 5. Orbital densities of an unreconstructed Si(100) surface along the plane shown in Fig. 1(c). The first 3.5 layers are shown. Dangling-bond- [(a), top row] and the dimer-surface-state bands [(b), second row] along the $J'\Gamma$ line in the irreducible quarter of the surface Brillouin zone [see Fig. 1(b)] for four selected parallel crystal momenta $\mathbf{k}_\parallel$. Atomic planes parallel to the surface are indicated by horizontal lines in (a),(b). The positions of the Si cores are shown as dots in (a), (b). In (c) and (d) the orbital densities of two surface-state resonances near the Γ point of surface Brillouin zone are represented.

split off the valence-band maximum and appears as a peak at 0.4–0.5 eV above the Fermi level. The dimer band is increasing its spectral weight near the conduction-band minimum at ≈ -2 eV. The narrow band of valence states between -8 and -4 eV is most important for the description of the charge transfer. The structures at low energies $E < -8$ eV are due to core localized bulk states. Even though these states are important for the screening of the Si ionic cores, they are

not relevant for the charge-transfer dynamics in the considered range of collision energies.

B. Scattered H$^-$ fraction

The outgoing negative ion fractions were obtained by solving Eqs. (28) for the transition amplitudes. Trajectories were evaluated for normal incidence using the Thomas-Fermi-Molière interatomic potential [21] at kinetic energies between 50 and 150 eV of the incoming projectiles. Table II gives the outgoing part of the scattering trajectories $D(t)$ for three incoming energies $E = 150$, 100, and 50 eV. The classical turning point of the trajectories is reached at $t=0$, and the distance between the surface and projectile is measured relative to the jellium edge at $D=0$. The classical trajectories are
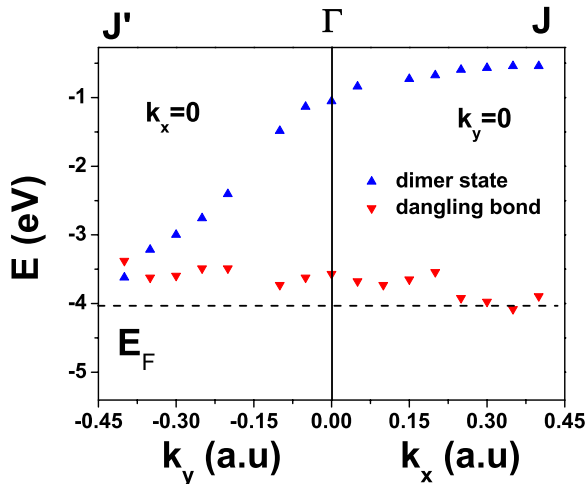

FIG. 6. (Color online) Dispersion of the two surface-state bands of unreconstructed Si(100) surface as a function of the parallel momentum $\mathbf{k}_\parallel = (k_x, k_y)$ along the $J'\Gamma J$ contour in the surface Brillouin zone [see Fig. 1(b)]. The negative values of k_y along the $J'\Gamma$ line correspond to decreasing momentum. Energy is measured relative to the vacuum energy level. The position of the Fermi level, $E_F = -4.1$ eV, is denoted by the dashed line.
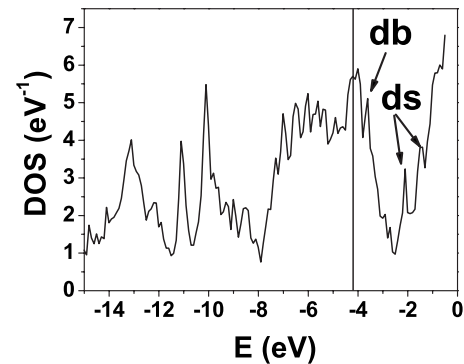

FIG. 7. Total density of states for the unreconstructed Si(100) surface, calculated using 3200 electronic states in the irreducible part of the surface Brillouin zone. Arrows indicate the dangling-bond (db) and dimer-state bands (ds).

TABLE II. Outgoing part of the trajectories for incident H⁻ ions backscattered from a Si(100) surface. The point of closest approach is reached at time $t=0$. D is the distance from the jellium edge of the surface and E is the incoming kinetic energy.

t (a.u.)		0	50	100	150	200	250
$E=150$ eV	D (a.u.)	0.2	3.0	6.9	10.8	14.7	18.6
$E=100$ eV	D (a.u.)	0.5	2.5	5.6	8.8	12.0	15.2
$E=50$ eV	D (a.u.)	1.1	2.2	4.3	6.5	8.7	10.9

calculated by solving Newton's equations of motion after averaging the Thomas-Fermi-Molière interatomic interactions between the projectile and individual Si atoms of the substrate over the surface plane ("planar average").

The couplings of the projectile affinity level to individual orbitals of the substrate are shown in Fig. 8 for four selected states at the Γ point ($\mathbf{k}_\parallel=0$) of SBZ, together with the phase portrait of the ion trajectories. The ion-surface interactions are oscillatory functions of the collision velocity and decay exponentially with the distance from the surface. However, the interaction range with the valence-, surface-, and conduction-band states is very different. The couplings to the valence-band states are usually localized at smaller distances $D<5$ in front of the surface [Fig. 8(a)]. The interactions with the dangling-bond surface states [cf. Fig. 5(a)] and dangling-bond surface-state resonances [cf. Figs. 5(c) and 5(d)] are dominant and exhibit pronounced long-range behavior, as shown in Fig. 8(b). The surface-aligned bridge states near the Γ point, exhibit short-range interactions with the atomic orbital [Fig. 8(c)]. The larger strength of their interactions distinguishes these states from the valence band. The couplings to the conduction band exhibit the longest interaction range, as Fig. 8(d) suggests.

The contributions to the evolving charge states of H⁻ are shown in Figs. 9(a)–9(c) for incident kinetic energies $E=150$, 100, and 50 eV, respectively. For all kinetic energies we observe a rapid decay of the initial negative-ion fraction due to electron loss to the conduction band of the surface. This loss is followed by capture from the valence band at large distances $D\approx6$–7 prior to reflection from the surface.

The affinity level of H⁻ is rapidly depleted at smaller distances $D<6$. As the projectile approaches the turning point, the capture probability approximately stabilizes for a time interval of about 70 a.u. After reflection from the surface, the H⁻ fraction continues to evolve, due to capture which occurs at distances between $D=4$ and 7. From the comparison of the results shown in Fig. 9, we also see that the final negative-ion yields are weakly dependent on the considered range of kinetic energies. The oscillations in the charge state of the decaying initial fraction prior to reflection are not physical, because the energy levels of the surface were calculated only up to the vacuum energy level. The major contribution to the final negative yield comes from the amplitudes S_{ak} for capture of a valence electron. These amplitudes are not sensitive to the high energy cutoff (i.e., the neglect of the unbound continuum part with $\varepsilon_k>0$) of the spectrum of the surface Hamiltonian. These contributions to the survival amplitude S_{aa} due to transition into and out of unbound continuum states were not studied here, in view of technical complications related to the proper definition of asymptotic scattering states within our finite-size slab calculations. Therefore, in our further analysis of numerical results, we will neglect the small contributions from the residual-ion amplitude S_{aa} all together and consider only the contributions S_{ak} from valence-electron capture.

In order to analyze this result, we show in Figs. 10(a) and 10(b) the amplitude $A_r=|\Sigma(t,t-\tau)|$ of the self-energy of an electron evolving into and out of the affinity level of the incident H⁻ ion with a kinetic energy of $E=150$ eV. Here $\tau\geq0$ is the time interval between the present and previous charge state of the projectile. We see that A_r is strongly peaked at equal times $\tau=0$ with a width of less than $\tau_c=50$ a.u., which is the characteristic correlation time over which the system holds memory of its previous state. Therefore long-time correlations are not relevant for the dynamics.

The peaking of the self-energy of the electron at equal times suggests that the adiabatic approximation may be applicable. For this approximation to be valid, the couplings $V_{ak}(t)$ must vary slowly on a time scale over which the kernel changes ($\tau_c<50$). Using the adiabatic approximation to Eq. (28), the ion-survival amplitude is given by
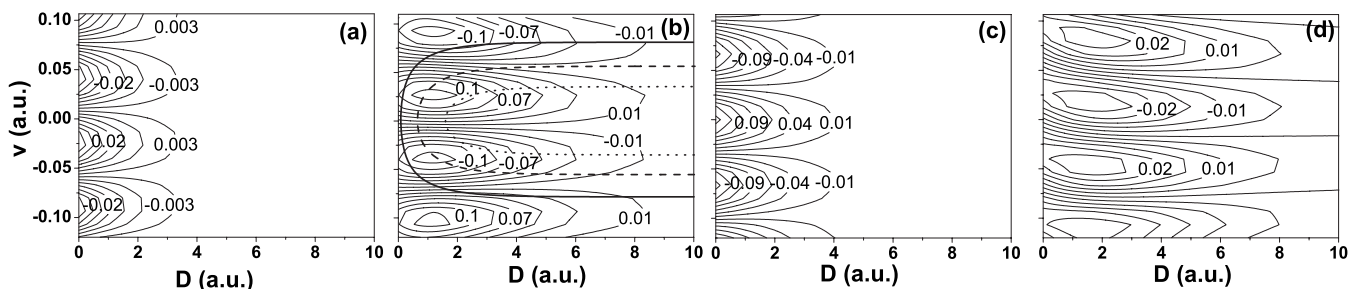

FIG. 8. Real part of the interactions $\mathrm{Re}[V_{ak}(D,v)]$ of the H⁻ affinity level orbital with the Kohn-Sham orbitals of an unreconstructed Si(100) surface. D is the ion-surface distance relative to the jellium edge and v is the velocity of the projectile along the surface normal. The couplings are shown near the Γ point of the surface Brillouin zone ($\mathbf{k}_\parallel=0$). (a) Interaction of the affinity level orbital with a state near the valence-band maximum. (b) Interaction with the dangling-bond surface state, together with the phase portrait of the classical trajectories for incident projectiles with kinetic energies of $E=150$ (solid), 75 (dashed), and 50 eV (dotted line). (c) Coupling to the dimer orbital. (d) Interaction with a conduction-band orbital.
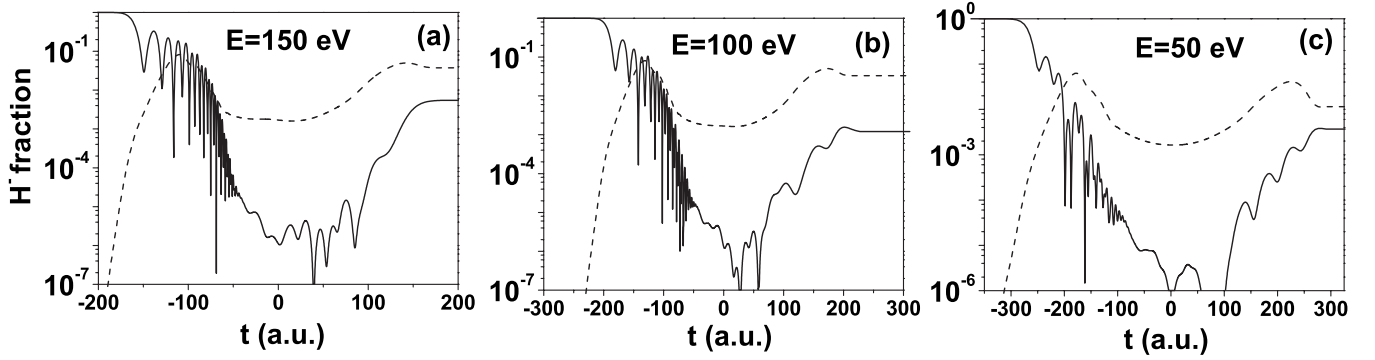
FIG. 9. Contributions to the H⁻ fraction near an unreconstructed Si(100) surface as a function of time for three different collision energies (a) 150 eV, (b) 100 eV, and (c) 50 eV. Negative times correspond to the incoming part of the trajectory. The point of closest approach is reached at $t=0$. The solid curve is the probability for survival of the initial H⁻ fraction [first term in Eq. (32)]. The dashed curve is the probability for capture of an electron from the valence band of the crystal into the affinity level of H⁻ [second term in Eq. (32)]. The sum of the two contributions gives the observable outgoing H⁻ yield (not shown).

$$S_{aa}(t) = \exp\left(-i \int_{t_0}^{t} d\tau \zeta_a(\tau)\right), \qquad (34)$$

where the resonance energy $\zeta_a(t) = \Lambda(t) - i\Delta(t)$ is expressed in terms of affinity level shift and width

$$\Lambda(t) = \sum_k \mathcal{P} \frac{1}{\varepsilon_a(t) - \varepsilon_k} |V_{ak}(t)|^2, \qquad (35)$$

$$\Delta(t) = \pi \sum_k \delta[\varepsilon_a(t) - \varepsilon_k] |V_{ak}(t)|^2 \qquad (36)$$

where $\mathcal{P}(1/x) = d\ln|x|/dx$. Both quantities are shown as a function of distance to the surface in Fig. 11(a). We see that the width of the affinity level resonance has a significant magnitude $\Delta=4$ eV at even larger distances $D=7$, i.e., the initial negative-ion fraction leaks rapidly into the conduction band of the surface, while the chemisorption shift Λ is almost negligible at such distances. Noticeably the width exhibits a strong dependence on the incoming kinetic energy of the projectile, and decreases rapidly as the velocity of the projectile decreases.

The same adiabatic approximation can be applied in order to obtain an analytic representation for the capture amplitudes S_{ak}, by expanding Eq. (28) in a perturbation series

$$S_{ak}(t) = S_{ak}^{(1)}(t) + S_{ak}^{(3)}(t) + \cdots, \qquad (37)$$

where $S_{ak}^{(1)} = -i \int^t \widetilde{V}_{ak}(t') dt'$ is the first-order capture amplitude. The next nonvanishing contribution in the perturbation series satisfies the equation

$$i\partial_t S_{ak}^{(3)} = \int^t \widetilde{\Sigma}_r(t,t') S_{ak}^{(1)}(t') dt'$$

$$= -\sum_j \widetilde{V}_{aj}(t) \int_{-\infty}^{t} dt' \, \widetilde{V}_{aj}^*(t') \int_{-\infty}^{t'} dt'' \widetilde{V}_{ak}(t''). \quad (38)$$

We take the slowly varying couplings V_{ak} outside the integrals to obtain

$$i\partial_t S_{ak}^{(3)} \approx -\frac{\widetilde{V}_{ak}(t)}{(\omega_{ak}+i0)} \sum_j \frac{|V_{aj}(t)|^2}{\omega_{kj}+i0} \approx S_{ak}^{(1)}(t)\zeta_{ak}(t), \quad (39)$$

where $\omega_{kj} = \varepsilon_k - \varepsilon_j$ are the unperturbed transition frequencies of the substrate. The complex frequencies

$$\zeta_{ak}(t) = \Lambda_{ak} - i\Delta_{ak} = \sum_j \frac{|V_{aj}(t)|^2}{\omega_{kj}+i0}. \qquad (40)$$

can be interpreted as collision-induced shifts Λ_{ak} and broadenings Δ_{ak} of the unperturbed transition frequencies $\omega_{ak}(t) = \varepsilon_a(t) - \varepsilon_k$. The shift Λ_{ak} describes a virtual transition of a valence electron into the affinity level of the negative ion. The broadening Δ_{ak} originates in indirect energy-conserving

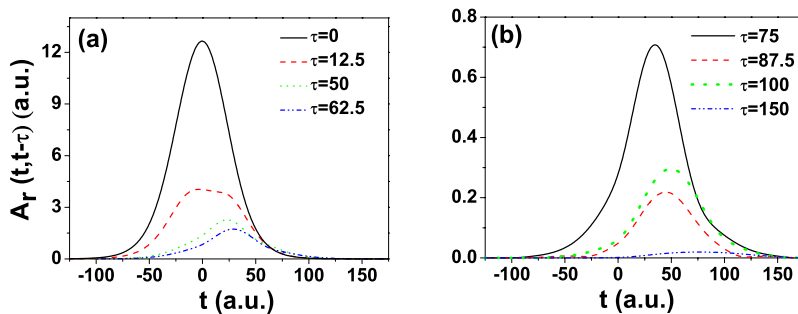

FIG. 10. (Color online) Amplitude $A_r(t, t-\tau)$ of the self-energy kernel relating the charge state of H⁻ near an unreconstructed Si(100) surface at two times t and $t-\tau$.
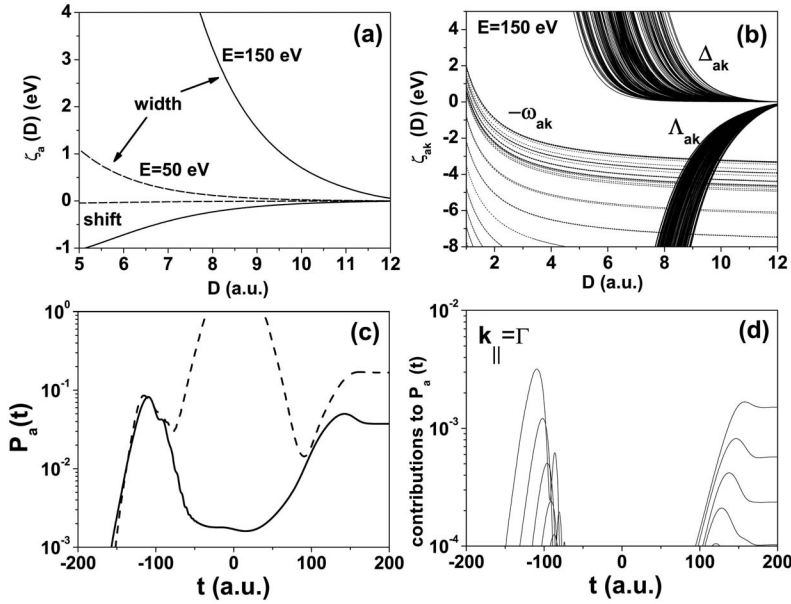
FIG. 11. Results for H⁻ interacting with an unreconstructed Si(100) surface. (a) Adiabatic shift and width of the affinity level resonance ζ_a for kinetic energies 150 eV (solid lines) and 50 eV (dashed lines) of the incident negative ion. (b) Adiabatic shifts Λ_{ak} and broadenings Δ_{ak} of the transition frequencies ω_{ka} (dashed lines) for incident 150 eV H⁻ ion. The distance D in (a) and (b) is measured relative to the jellium edge. (c) Comparison of the H⁻ fraction calculated by direct numerical integration of the Newns-Anderson model (solid line) with our adiabatic approximation (dashed line). (d) Individual contributions to the H⁻ formation probability from eight valence states near the Γ point of the surface Brillouin zone, calculated by direct numerical integration of the Newns-Anderson model.

transitions between the highly degenerate band states of the substrate. These shifts and broadenings are shown in Fig. 11(b) for $-0.3 < \varepsilon_k < \varepsilon_F \approx -0.15$. We see that both quantities are highly dispersed and vary rapidly with the distance from the surface D.

If the perturbative expansion is carried to infinite order, it is easy to verify by induction that

$$i\partial_t S_{ak}(t) = \zeta_{ak}(t) S_{ak}(t) + \tilde{V}_{ak}(t). \tag{41}$$

Therefore, the amplitudes for electron capture

$$S_{ak} = \int_{t_0}^{\infty} dt' V_{ak}(t') G_{ak}(t,t'), \tag{42}$$

describe excitation and propagation of resonances that evolve from the substrate into the adiabatically shifted affinity level $\varepsilon_a(t)$ of the negative ion. The Green's functions

$$G_{ak}(t,t') = -i\theta(t-t')\exp\left(-i\int_{t'}^{t} d\tau[\omega_{ak} + \zeta_{ak}(\tau)]\right), \tag{43}$$

are the propagators of these resonance states. In our further analysis we will refer to Eq. (42) as adiabatic approximation.

We first show that (i) the adiabatic approximation is appropriate for a qualitative discussion of the numerical results and (ii) only selected substrate states can stimulate electron capture into the affinity level of the negative ion. In Fig. 11(c) we compare our numerical results in adiabatic approximation with our numerical solution of the Newns-Anderson model given by Eq. (28) for incident H⁻ with kinetic energies of 150 eV. As the comparison suggests the adiabatic approximation can explain well the numerical data on both the incoming and outgoing part of the projectile's trajectory. At small distances form the surface the direct numerical integration of the Newns-Anderson model differs significantly from the adiabatic approximation. This difference occurs because the collision-induced broadening Δ_{ak} is very large at small

distances to the surface, making the numerical integration difficult. However, the numerical distortion of the adiabatic approximation at these distances is not relevant since electron capture on the incoming and outgoing part of the trajectory are separated by a large time interval $\tau > 50$. This interval is larger than the memory range of the self-energy kernel τ_c. Therefore, electron capture on the incoming and outgoing part of the trajectory are not related. This is in agreement with the observation by Maazouz et al.[1] of the complete loss of memory of the initial charge states. Individual contributions to the electron capture probability $P_a(t)$ near the Γ point of SBZ, obtained after direct integration of Eqs. (28) are shown in Fig. 11(d) for a group of eight occupied valence states below the Fermi level. We see that dominant contributions to $P_a(t)$ are coming from the two dangling-bond surface-state resonances, which exhibit strong and long-range interactions with the negative-ion affinity level [cf. Fig.8(b) and Figs. 5(c) and 5(d)].

In order to rationalize this result we make use of the adiabatic approximation. In Fig. 12(a) we show the collisional shifts Λ_{ak} and broadenings Δ_{ak} of two electronic transitions that occur for $\mathbf{k}_\parallel = \Gamma$ at a collision energy of 150 eV. The first state $|u\rangle$ is the surface-state resonance shown in Fig. 5(c) with energy $\varepsilon_u \approx -0.2$. The second state $|l\rangle$ is a deep valence-band level with orbital energy $\varepsilon_l = -0.5$. We drop the index "a" in what follows in order to simplify the notation. The broadenings $\Delta_{l,u}$ become very large close to the jellium edge, i.e., $\Delta_l = 8$ eV at $D = 3.5$ and $\Delta_u = 8$ eV at $D = 6$. Therefore these excitations can evolve only at large distances from the surface. The shifts Λ exhibit significant magnitudes at large distances from the surface, i.e., at physisorption distances. For example, $\Lambda_l \approx \Lambda_u \approx 3$ eV at $D = 9$. At distances, where the energy $\Lambda_{l,u}$ carried by the excitations is close to or matches the transition frequency $-\omega_{l,u}$, the phase factor in Eqs. (42) and (43) varies slowly. This gives the major contribution to the transition amplitudes $S_{l,u}$. The energy-matching distances are $D_l = 6$ and $D_u = 8.5$ for the lower and the upper transitions, respectively. Therefore, in order for the
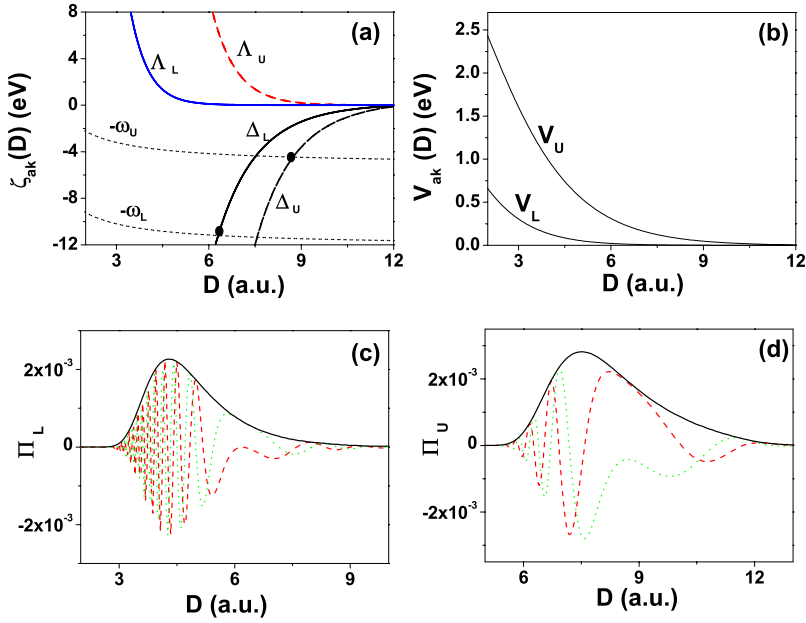
FIG. 12. (Color online) (a) Collisional shifts Λ_l and Λ_u and widths Δ_l and Δ_u for two transition frequencies ω_l and ω_u for H$^-$ colliding with an unreconstructed Si(100) surface at a kinetic energy of 150 eV. (b) Coupling strengths $|V_l|$ and $|V_u|$ relevant for transitions from the states $|l\rangle$ and $|u\rangle$ into the affinity level of H$^-$. (c) Contribution Π_l to the electron capture amplitude from the state $|l\rangle$ with energy $\varepsilon_l = -0.5$. (d) Contribution Π_u to the electron capture amplitude from the state $|u\rangle$ with energy $\varepsilon_u = -0.22$ (see text). The dotted lines in (c) and (d) indicate the real part of $\Pi_{l,u}$. The dashed lines are the imaginary parts of $\Pi_{l,u}$. Solid lines indicate the envelopes $|\Pi_{l,u}|$.

transitions to occur, the couplings must exhibit long range.

The couplings V_l and V_u relevant for the two transitions are shown in Fig. 12(b). The upper transition, which is stimulated by the interaction of the affinity level with the surface-state resonance, is long ranged, while the lower transition exhibits a shorter interaction range. The integrands $\Pi_{l,u}(t_2) = G_{l,u}(t_1, t_2)\exp[-i\omega_{l,u}(t_1 - t_2)]V_{l,u}(t_2)$ for $t_1 \to \infty$ in Eqs. (42) and (43) are shown in Figs. 12(c) and 12(d) as a function of the distance from the surface, respectively. The lower transition is less likely to occur, as Fig. 12(c) shows. This is because before the energy-matching condition $\Lambda_l \approx -\omega_l$ is satisfied, the phase factor changes rapidly, which leads to the cancellation of the contributions from V_l until $D \approx D_l$. Hence a narrow region of less than 2 a.u. near D_l gives the main contribution to the integral where, however, the coupling V_l is very weak. In contrast, a wider region of distances $D = 7-11$ contributes to electron capture for the upper transition as shown in Fig. 12(d). The phase is nearly stationary over this interval of distances, and the contribution to the amplitude S_u after integration is evidently much larger. The effects of the nonorthogonality between the basis states in our scattering calculations (i.e., $N_{ak} = \langle a|k\rangle \neq 0$) would change the effective couplings V_{ak}. This effect would be stronger at smaller distances from the surface, where the collision-induced broadenings Δ_{ak} are large and no charge transfer occurs. At larger distances $D > 6$, where formation of H$^-$ states is favored, the effects of the overlap are weakened, and one may expect that long-range couplings to surface states are not significantly altered by orthogonalization effects.

The negative-ion fractions calculated from the direct numerical integration of the Newns-Anderson model are shown in Fig. 13 as a function of the incident velocity of the H$^-$ ion in comparison with experimental data of Maazouz [1] for scattering of hydrogen atoms on Si surfaces for incident energies of 1 keV and various angles of incidence. Even though our results overestimate the experiment, the theoret-

ical negative-ion fraction decreases as the impact velocity is lowered. A similar trend is observed in the experimental data. The theoretical results in Ref. [3] are in much better agreement with the experiment as the perpendicular velocity v_p becomes smaller. However, their results start to systematically deviate from the experiment at higher v_p. The smoother variation of our fraction with increasing v_p tends to agree better with the experimental results of Maazouz *et al.* Therefore, we provide evidence for a realistic description of charge transfer near a silicon surface, even though our model does not include the effects of the surface reconstruction and parallel motion of the projectile.
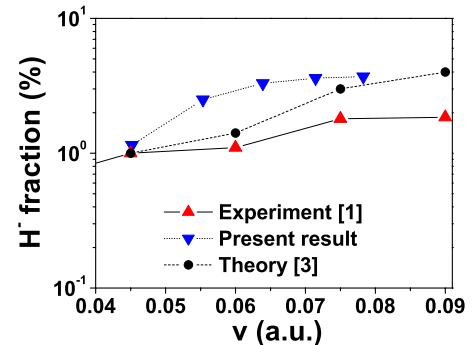

FIG. 13. (Color online) Outgoing H$^-$ fraction after collision with an unreconstructed Si(100) surface as a function of the normal velocity of the projectile. Triangles represent experimental results of Maazouz *et al.* [1] for the outgoing H$^-$ fraction for incident H atoms with kinetic energies of 1 keV and for various incidence angles. The inverted triangles are our theoretical results for normally incident H$^-$ ions. Circles represent theoretical H$^-$ fractions calculated by E. A. Garcia *et al.* for 1 keV hydrogen atoms incident on a Si(111)7×7 surface.

IV. CONCLUSION

We have calculated *ab initio* the outgoing H⁻ fraction after backscattering of normally incident H⁻ ions with kinetic energies between 50 and 150 eV on an unreconstructed Si(100) surface. We show that the final negative-ion fraction evolves from the Fermi sea of the substrate by nonresonant capture of an electron from dangling-bond surface-state resonances into the affinity level of H⁻. Our results for the dependence of the negative-ion fraction on the velocity component normal to the surface are in qualitative agreement with the experiment of Ref. [1]. The remaining difference may be due to effects of the nonvanishing orbital overlap, surface reconstruction, and trajectory-dependent parallel-velocity effects. We intend to address these effects, while making reference to results of our present work.

ACKNOWLEDGMENTS

APPENDIX A: WANG-TETER CORRECTIONS AND FITTING FUNCTIONS

The Wang-Teter kinetic energy is a sum of two terms, $T_{WT} = T_1 + T_2$. T_1 and T_2 are the linear and quadratic response contributions. The variational derivative of T_1 is $\delta T_1 / \delta n(\mathbf{r}) = 5/6 n^{-1/6}(\mathbf{r}) \widetilde{\mathcal{F}}[\delta T_1 / \delta n_{\mathbf{G}}^{(5/6)}] = 5/6 n^{-1/6}(\mathbf{r}) \widetilde{\mathcal{F}}[K_s(G) n_{-\mathbf{G}}^{(5/6)}]$, where $\mathbf{G}$ are the reciprocal lattice wave-vectors. $\mathcal{F}$ and $\widetilde{\mathcal{F}}$ denote forward and inverse Fourier transformations, respectively. The source term j_s in Eq. (15) requires the evaluation of the derivative of T_2 in momentum space $\delta T_2 / \delta n_{\mathbf{G}} = 5/9 \mathcal{F}\{n^{-4/9}(\mathbf{r}) \widetilde{\mathcal{F}}[\delta T_2 / \delta n_{\mathbf{G}}^{(5/9)}]\}$. In order to evaluate this derivative, the three-point kernel is approximated as

$$L_s(x_1, x_2, x_3) \approx \Gamma(x_1, x_2, x_3) \sum_{t=1}^{4} f_{i_t}(x_1) f_{j_t}(x_2) f_{k_t}(x_3), \quad \text{(A1)}$$

where $x_i = G_i / k_F$. $\{f_i(x), i = 1, \ldots, 7\}$ are the Wang-Teter screening functions, introduced to factorize the nonseparable analytic dependence of the wave vectors in Eq. (12). The three-point function Γ is

$$\Gamma(x_1, x_2, x_3) = -\frac{13}{540} - \frac{1}{120}\left(\frac{x_1^4}{x_2^2 x_3^2} + \frac{x_2^4}{x_1^2 x_3^2} + \frac{x_3^4}{x_1^2 x_2^2} - \frac{x_2^2 x_1^2}{x_1^2 x_2^2} - \frac{x_2^2}{x_3^2}\right.$$
$$\left. - \frac{x_3^2}{x_2^2} - \frac{x_1^2}{x_3^2} - \frac{x_3^2}{x_1^2}\right). \quad \text{(A2)}$$

Explicit expressions for the functions f_i are given in [7,8]. The representation (A1) leads to the variational derivative

$$\frac{\delta T_2[n]}{\delta n^{(5/9)}(\mathbf{G})} = -\frac{729 k_F^2}{125 n_0^{2/3}} \left\{ \frac{f_1(x)}{20} \left[\frac{-13}{9} G_1(\mathbf{G}) - \frac{1}{x^2} G_2(\mathbf{G}) \right. \right.$$
$$\left. - \frac{x^4}{2} G_3(\mathbf{G}) + G_4(\mathbf{G}) - \frac{1}{x^2} G_5(\mathbf{G}) + x^2 G_6(\mathbf{G}) \right]$$
$$+ 3 f_2(x) [2 G_7(\mathbf{G}) + f_3(x) G_8(\mathbf{G})] + 6 f_4(x) G_9(\mathbf{G})$$
$$+ 3 f_5(x) G_{10}(\mathbf{G}) + 6 f_7(x) G_{11}(\mathbf{G})$$
$$\left. + 3 f_6(x) G_{12}(\mathbf{G}) \right\}, \quad \text{(A3)}$$

where the functions $G_i(\mathbf{G})$ are defined in Ref. [8] as

$$G_1(\mathbf{G}) = \mathcal{F}[F_1(\mathbf{r})^2],$$

$$G_2(\mathbf{G}) = \mathcal{F}[F_2(\mathbf{r}) F_3(\mathbf{r})],$$

$$G_3(\mathbf{G}) = \mathcal{F}[F_3(\mathbf{r})^2],$$

$$G_4(\mathbf{G}) = \mathcal{F}[F_4(\mathbf{r}) F_3(\mathbf{r})],$$

$$G_5(\mathbf{G}) = \mathcal{F}[F_4(\mathbf{r}) F_1(\mathbf{r})],$$

$$G_6(\mathbf{G}) = \mathcal{F}[F_3(\mathbf{r}) F_1(\mathbf{r})],$$

$$G_7(\mathbf{G}) = \mathcal{F}[F_5(\mathbf{r}) F_6(\mathbf{r})],$$

$$G_8(\mathbf{G}) = \mathcal{F}[F_6^2(\mathbf{r})],$$

$$G_9(\mathbf{G}) = \mathcal{F}[F_7(\mathbf{r}) F_8(\mathbf{r})],$$

$$G_{10}(\mathbf{G}) = \mathcal{F}[F_8^2(\mathbf{r})],$$

$$G_{11}(\mathbf{G}) = \mathcal{F}[F_9(\mathbf{r}) F_{10}(\mathbf{r})],$$

$$G_{12}(\mathbf{G}) = \mathcal{F}[F_{10}(\mathbf{r})^2]. \quad \text{(A4)}$$

The corresponding real-space functions F_i are given by the expressions

$$F_1(\mathbf{r}) = \widetilde{\mathcal{F}}[n_{\mathbf{G}}^{(5/9)} f_1(x)],$$

$$F_2(\mathbf{r}) = \widetilde{\mathcal{F}}[n_{\mathbf{G}}^{(5/9)} f_1(x) x^4],$$

$$F_3(\mathbf{r}) = \widetilde{\mathcal{F}}\left[n_{\mathbf{G}}^{(5/9)} \frac{f_1(x)}{x^2}\right],$$

$$F_4(\mathbf{r}) = \widetilde{\mathcal{F}}[n_{\mathbf{G}}^{(5/9)} f_1(x) x^2],$$

$$F_5(\mathbf{r}) = \widetilde{\mathcal{F}}[n_{\mathbf{G}}^{(5/9)} f_2(x) f_3(x)],$$

$$F_6(\mathbf{r}) = \widetilde{\mathcal{F}}[n_{\mathbf{G}}^{(5/9)} f_2(x)],$$

$$F_7(\mathbf{r}) = \widetilde{\mathcal{F}}[n_{\mathbf{G}}^{(5/9)} f_5(x)],$$

$$F_8(\mathbf{r}) = \tilde{\mathcal{F}}[n_\mathbf{G}^{(5/9)}f_4(x)],$$

$$F_9(\mathbf{r}) = \tilde{\mathcal{F}}[n_\mathbf{G}^{(5/9)}f_6(x)],$$

$$F_{10}(\mathbf{r}) = \tilde{\mathcal{F}}[n_\mathbf{G}^{(5/9)}f_7(x)]. \tag{A5}$$

The "wave function" of the ground-state electronic density is expanded in plane waves,

$$\psi(\mathbf{r}) = \frac{1}{\sqrt{\Omega}}\sum_\mathbf{G} e^{i\mathbf{G}\cdot\mathbf{r}}c_\mathbf{G}, \tag{A6}$$

and the equations for the coefficients are solved by iteration,

$$(1 + D\delta t/2)c_\mathbf{G}^{(m+1)} = 2c_\mathbf{G}^{(m)} - (1 - D\delta t/2)c_\mathbf{G}^{(m-1)}$$
$$- (\varphi_\mathbf{G}^{(m)} - \mu^{(m)}c_\mathbf{G}^{(m)})\delta t. \tag{A7}$$

m denotes the number of the iteration, $\varphi_\mathbf{G} = \mathcal{F}\{\psi(\mathbf{r})\mathcal{F}^{-1}[\delta T_{WT}/\delta n_\mathbf{G}]\} + \sum_{\mathbf{G}'}H[\psi; \mathbf{G} - \mathbf{G}']c_{\mathbf{G}'}$, H is the effective TFvW Hamiltonian on the left-hand side of Eq. (15), $D = 1.0$ is a damping coefficient, and the propagation time step $\delta t = 0.05$ was found to be adequate for convergence. The chemical potential is updated from

$$\mu^{(m)} = \frac{\langle\psi^{(m)}|\varphi^{(m)}\rangle}{\langle\psi^{(m)}|\psi^{(m)}\rangle}. \tag{A8}$$

The iterations of Eq. (A7) continue until the residual of the wave function becomes sufficiently small.

APPENDIX B: KOHN-SHAM EQUATIONS

Following Ref. [26], we implement the Car-Parrinello method [16] to solve Kohn-Sham equations (19). In this method the orbitals satisfy a system of coupled Euler-Lagrange equations of motion,

$$\partial_t^2\varphi_k(t) = -[H_{KS} - \varepsilon_k(t)]\varphi_k(t) + \sum_{l\neq k}\Lambda_{kl}(t)\varphi_l(t), \tag{B1}$$

where H_{KS} is the Kohn-Sham Hamiltonian and $k = \{\nu, \mathbf{k}\}$. The Langrangian multipliers ε_k correspond to orbital energies and the orbital couplings Λ_{kl} derive from the constraints of orthogonality $\langle\varphi_k|\varphi_l\rangle = \delta_{kl}$. In practice we propagate the partially constrained equations of motion for small time steps δt, i.e.,

$$\partial_t^2\varphi_k(t) = -[H_{KS} - \varepsilon_k(t)]\varphi_k(t), \quad t - \delta t \leq t \leq t + \delta t, \tag{B2}$$

where $\varepsilon_k = \langle\varphi_k|H_{KS}|\varphi_k\rangle/\langle\varphi_k|\varphi_k\rangle$. Next we impose the orthogonality constraints using the Gram-Schmidt procedure,

$$|\varphi_k\rangle \leftarrow \frac{|\varphi_k\rangle}{\langle\varphi_k|\varphi_k\rangle} - \sum_{l<k}\frac{\langle\varphi_l|\varphi_k\rangle}{\langle\varphi_l|\varphi_l\rangle}|\varphi_l\rangle. \tag{B3}$$

An orbital is considered as converged and excluded from the propagation (B2), if the Euclidean norm of the residual R_k has become sufficiently small, i.e.,

$$\|R_k\|_2 = \|(H_{KS} - \varepsilon_k)\varphi_k\|_2 < \varepsilon. \tag{B4}$$

Exploiting the periodicity of the crystal slab geometry used in our calculations, the orbitals are expanded over the reciprocal lattice wave vectors $\mathbf{G}$,

$$\varphi_{\nu,\mathbf{k}}(\mathbf{r},t) = \frac{1}{\sqrt{\Omega}}\sum_\mathbf{G} c_{\nu,\mathbf{k}+\mathbf{G}}(t)e^{i(\mathbf{k}+\mathbf{G})\cdot\mathbf{r}} \tag{B5}$$

where $\mathbf{k} = (\mathbf{k}_\parallel, 0)$. The addition of a small friction term of the form $\gamma_{\nu,\mathbf{k}}\dot{c}_{\nu,\mathbf{k}+\mathbf{G}}$ and substituting the plane-wave expansion in Eq. (B2) leads to a set of coupled equations for the dynamics of the coefficients

$$\ddot{c}_{\nu,\mathbf{k}+\mathbf{G}} + \gamma_{\nu,\mathbf{k}+\mathbf{G}}\dot{c}_{\nu,\mathbf{k}+\mathbf{G}} + \omega_{\nu,\mathbf{k}+\mathbf{G}}^2 c_{\nu,\mathbf{k}+\mathbf{G}} = -B_{\nu,\mathbf{k}+\mathbf{G}}, \tag{B6}$$

where

$$\omega_{\nu,\mathbf{k}+\mathbf{G}}^2 = \frac{1}{2}|\mathbf{k}+\mathbf{G}|^2 - \varepsilon_\nu(\mathbf{k}), \quad \gamma_{\nu,\mathbf{k}+\mathbf{G}} = D|\omega_{\mathbf{k}+\mathbf{G}}|. \tag{B7}$$

D is an infinitesimal damping constant and the driving "forces" are

$$B_{\nu,\mathbf{k}+\mathbf{G}} = \sum_\mathbf{G} v_s(\mathbf{G} - \mathbf{G}')c_{\nu,\mathbf{k}+\mathbf{G}'}. \tag{B8}$$

After specifying the initial conditions $\{t = t_0 | c_{\nu,\mathbf{k}+\mathbf{G}} = c_{\nu,\mathbf{k}+\mathbf{G}}^{(0)}, \dot{c}_{\nu,\mathbf{k}+\mathbf{G}} = \dot{c}_{\nu,\mathbf{k}+\mathbf{G}}^{(0)}\}$, the Eqs. (B6) together with the constraints (B3) are propagated numerically up to $t = T$, such that Eq. (B4) is satisfied for each ν, i.e.,

$$B_{\nu,\mathbf{k}+\mathbf{G}}(T) = \omega_{\nu,\mathbf{k}+\mathbf{G}}^2(T)c_{\nu,\mathbf{k}+\mathbf{G}}(T), \tag{B9}$$

and the matrix representation of the Hamiltonian H_{KS} in Eq. (19) is diagonal. The wave functions $\varphi_{\nu,\mathbf{k}}$ are stationary. For a small time step δt, Eqs. (B6) can be integrated analytically if the variation of the forces B_ν may be ignored. The solution of Eq. (B6) is

$$c_{\nu,\mathbf{k}+\mathbf{G}}(\delta t) = e^{-\gamma_{\nu,\mathbf{k}+\mathbf{G}}\delta t}[2\cos(\omega_{\nu,\mathbf{k}+\mathbf{G}}\delta t)c_{\nu,\mathbf{k}+\mathbf{G}}(0) - c_{\nu,\mathbf{k}+\mathbf{G}}$$
$$\times(-\delta t)] + [1 + e^{-2\gamma_{\nu,\mathbf{k}+\mathbf{G}}\delta t} - 2e^{-2\gamma_{\nu,\mathbf{k}+\mathbf{G}}\delta t}$$
$$\times\cos(\omega_{\nu,\mathbf{k}+\mathbf{G}}\delta t)]\frac{B_{\nu,\mathbf{k}+\mathbf{G}}}{\omega_{\nu,\mathbf{k}+\mathbf{G}}^2}. \tag{B10}$$

After each propagation time step, the constraints of orthogonality (B3) are imposed, new initial conditions are calculated, and the next propagation step is executed. The propagation time step $\delta t = 0.12$ and damping constant $D = 0.04$ were found to be adequate. More than 50 000 small time steps were necessary to converge the residuals to an accuracy of $\varepsilon = 0.000\,05$.

APPENDIX C: NEWNS-ANDERSON MODEL

The equations for the transition amplitudes are the Voltera equations (see also [27])

$$\partial_t\varphi = \int_{t_0}^t dt' K(t,t')\varphi(t') + g(t), \quad \varphi(t_0) = \varphi_0. \tag{C1}$$

Since the kernel is nearly singular and strongly peaked at equal times $t = t'$, we regularize Eq. (C1) by change of variables $\tau = 1/(1 + \exp[-\lambda(t - t_c)])$ and obtain

$$\partial_\tau \varphi = \int_0^\tau d\tau' J(\tau) K(\tau,\tau') J(\tau') \varphi(\tau') + g(\tau) J(\tau), \quad \text{(C2)}$$

where $\tau \in [0,1]$ and $J(\tau) = 1/[\lambda\tau(1-\tau)]$ is the Jacobian of the transformation. t_c is the point of closest approach and $\lambda^{-1} \approx 25$ is the characteristic time interval over which the kernel changes near the point of closest approach. The trans-formed equation has end-point singularities, which are unimportant since the couplings to the substrate vanish as $\tau \to 0,1$.

We discretize these equations on an uniform mesh with time step $\delta\tau = 0.0001$, evaluate the derivative using a two-point finite difference approximation, and use a trapezoidal rule to calculate the integrals.

[1] M. Maazouz, L. Guillemot, V. A. Esaulov, and D. J. O'Connor, Surf. Sci. **398**, 49 (1998).

[2] A. G. Borisov, D. Teillet-Billy, and J. P. Gauyacq, Phys. Rev. Lett. **68**, 2842 (1992).

[3] E. A. Garcia, C. González, P. G. Bolcato, M. C. G. Passegi, and E. C. Goldberg, Surf. Sci. **600**, 2195 (2006).

[4] J. P. Gauyacq and A. G. Borisov, J. Phys.: Condens. Matter **10**, 6585 (1998).

[5] P. Honenberg and W. Kohn, Phys. Rev. **136**, B864 (1964).

[6] M. Schlüter, J. R. Chelikowsky, S. G. Louie, and M. L. Cohen, Phys. Rev. B **12**, 4200 (1975).

[7] L. W. Wang and M. P. Teter, Phys. Rev. B **45**, 13196 (1992).

[8] M. Foley and P. A. Madden, Phys. Rev. B **53**, 10589 (1996).

[9] Y. A. Wang, N. Govind, and E. A. Carter, Phys. Rev. B **58**, 13465 (1998).

[10] T. J. Frankcombe, G. J. Kroes, N. I. Choly, and E. Kaxiras, J. Phys. Chem. B **109**, 16554 (2005).

[11] R. M. Dreitzler and E. K. U. Gross, *Density Functional Theory* (Springer, Berlin, 1990).

[12] W. Kohn and L. J. Sham, Phys. Rev. **140**, A1133 (1965).

[13] A. L. Fetter and J. W. Walecka, *Quantum Theory of Many-Particle Systems.* (McGraw-Hill, New York, 1971).

[14] J. M. Pitarke, R. H. Ritchie, and P. M. Echenique, Phys. Rev. B **52**, 13883 (1995).

[15] B. Obreshkov and U. Thumm, Phys. Rev. A **74**, 012901 (2006).

[16] R. Car and M. Parrinello, Phys. Rev. Lett. **55**, 2471 (1985).

[17] R. Brako and D. M. Newns, Rep. Prog. Phys. **52**, 665 (1989).

[18] J. S. Cohen and G. Fiorentini, Phys. Rev. A **33**, 1590 (1986).

[19] L. V. Keldysh, Sov. Phys. JETP **20**, 1018 (1965).

[20] N. W. Ashcroft and N. D. Mermin, *Solid State Physics*, (Thomson Learning Inc., London, 1976).

[21] B. Obreshkov and U. Thumm, Surf. Sci. **601**, 622 (2007).

[22] F. J. Himpsel and D. E. Eastman, J. Vac. Sci. Technol. **16**, 1297 (1979).

[23] R. G. Musket and M. Balooch, J. Vac. Sci. Technol. A **20**, 2049 (2002).

[24] J. A. Appelbaum, G. A. Baraff, and D. R. Hamann, Phys. Rev. B **11**, 3822 (1975).

[25] G. P. Kerker, S. G. Louie, and M. L. Cohen, Phys. Rev. B **17**, 706 (1978).

[26] M. Payne, M. P. Teter, D. C. Allan, T. A. Arias, and J. D. Joannopoulos, Rev. Mod. Phys. **64**, 1045 (1992).

[27] W. H. Press, S. A. Teukolsky, W. T. Vetterling, and B. P. Flannery, *Numerical Recipes in FORTRAN* (Cambridge University Press, Cambridge, England, 1993).